



# A novel MoS<sub>2</sub> quantum dots (QDs) decorated Z-scheme g-C<sub>3</sub>N<sub>4</sub> nanosheet/N-doped carbon dots heterostructure photocatalyst for photocatalytic hydrogen evolution

Yingying Jiao<sup>a</sup>, Qunzeng Huang<sup>b</sup>, Jianshe Wang<sup>a,\*</sup>, Zhanhang He<sup>a,\*</sup>, Zhongjun Li<sup>a,\*</sup>

<sup>a</sup> College of Chemistry and Molecular Engineering, Zhengzhou University, Zhengzhou 450001, PR China

<sup>b</sup> College of Chemistry and Pharmaceutical Engineering, Engineering Technology Research Center of Henan Province for Solar Catalysis, Nanyang Normal University, Nanyang 473061, PR China

## ARTICLE INFO

### Keywords:

Carbon nitride  
N-doped carbon dots  
MoS<sub>2</sub>QDs  
Z-scheme heterojunction  
Photocatalytic hydrogen evolution

## ABSTRACT

A novel MoS<sub>2</sub> quantum dots (QDs) decorated g-C<sub>3</sub>N<sub>4</sub> nanosheet/N-doped carbon dots (NCDS) heterojunction photocatalyst was successfully synthesized by thermal polymerization and subsequent solvothermal approach. Under visible light ( $\lambda \geq 420$  nm) irradiation, the as-prepared g-C<sub>3</sub>N<sub>4</sub>/NCDS/MoS<sub>2</sub> composite with 3wt% of MoS<sub>2</sub> and 2wt% of NCDS displayed the highest photocatalytic hydrogen evolution activity with a corresponding H<sub>2</sub> evolution rate of 212.41  $\mu\text{mol g}^{-1} \text{h}^{-1}$ , which was about 53 times higher than that of g-C<sub>3</sub>N<sub>4</sub>/MoS<sub>2</sub>-3%. Moreover, the g-C<sub>3</sub>N<sub>4</sub>/NCDS/MoS<sub>2</sub> composite exhibited excellent photostability. The enhanced photocatalytic activity of g-C<sub>3</sub>N<sub>4</sub>/NCDS/MoS<sub>2</sub> composite was predominantly attributed to the formation of Z-scheme heterojunction between g-C<sub>3</sub>N<sub>4</sub> and NCDS, which effectively accelerated the transfer and separation of photogenerated charge carriers. Besides, the introduction of noble metal-free MoS<sub>2</sub> co-catalyst further promoted the separation of photogenerated charge carriers and provided more active sites for H<sub>2</sub> evolution reaction. The advantages of superior photocatalytic activity and excellent stability endowed a promising potential for g-C<sub>3</sub>N<sub>4</sub>/NCDS/MoS<sub>2</sub> composite to apply in photocatalytic fields.

## 1. Introduction

Since Antonietti et al. initially reported that graphite carbon nitride (g-C<sub>3</sub>N<sub>4</sub>) was active for water splitting, it has attracted tremendous attentions due to its relatively narrow band gap, proper band edges, cost effectiveness and excellent chemical stability [1–3]. However, the high recombination rate of photogenerated carriers constrains its photocatalytic activity and wide application [4–6]. To address this issue, different strategies have been developed, including element doping [7], heterojunction constructing [8] and nanostructure controlling [9,10]. Among these strategies, constructing heterojunction is considered to be one of the most effective ways. So far, various heterojunctions have been constructed, such as semiconductor/g-C<sub>3</sub>N<sub>4</sub> junction (TiO<sub>2</sub>/g-C<sub>3</sub>N<sub>4</sub> [11], BiOBr/g-C<sub>3</sub>N<sub>4</sub> [12], ZnS/g-C<sub>3</sub>N<sub>4</sub> [13], CoP/g-C<sub>3</sub>N<sub>4</sub> [14]), polymer/g-C<sub>3</sub>N<sub>4</sub> junction (C<sub>3</sub>N<sub>4</sub>-PEDOT-Pt [15]), carbon/g-C<sub>3</sub>N<sub>4</sub> junction (carbon dots/g-C<sub>3</sub>N<sub>4</sub> [16,17], carbon/g-C<sub>3</sub>N<sub>4</sub> nanofibers [18], carbon framework/g-C<sub>3</sub>N<sub>4</sub> [19], carbon ring/g-C<sub>3</sub>N<sub>4</sub> [20]). Among them, carbon dots/g-C<sub>3</sub>N<sub>4</sub> heterojunction, due to the characteristic of carbon dots such as chemical stability, low cost, unique light induced

electron transfer and electron storage properties, is regarded as one of the most promising materials for water splitting [21]. Although the performance of carbon dots/g-C<sub>3</sub>N<sub>4</sub> is impressive, the most disadvantage is the involving of noble metals such as Pt [22], Pd and Au [23]. Therefore, it is of great significant to develop g-C<sub>3</sub>N<sub>4</sub> based composite photocatalysts with high performance without using noble metals.

Molybdenum disulfide (MoS<sub>2</sub>) has unique structure with the unsaturated atoms of both Mo and S at the edges, which can provide favorable edge activity during the catalytic process. Recent researches have shown that MoS<sub>2</sub> can be used as an effective co-catalyst for photocatalytic hydrogen evolution [24–32]. For instance, Zhao et al. [33] and Hou et al. [24] reported g-C<sub>3</sub>N<sub>4</sub>/MoS<sub>2</sub> and g-C<sub>3</sub>N<sub>4</sub>/graphene/MoS<sub>2</sub> composite photocatalysts and investigated their photocatalytic hydrogen evolution activity, respectively. Wang et al. reported self-optimization of the active site of molybdenum disulfide by an irreversible phase transition during photocatalytic hydrogen evolution [34]. Up to now, most studies are confined to MoS<sub>2</sub> nanosheet co-catalyst. Compared with monolayered MoS<sub>2</sub>, more unsaturated terminal sulfur atoms

\* Corresponding authors.

E-mail addresses: [jianshewang@zzu.edu.cn](mailto:jianshewang@zzu.edu.cn) (J. Wang), [hezhanhang@139.com](mailto:hezhanhang@139.com) (Z. He), [lizhongjun0713@163.com](mailto:lizhongjun0713@163.com) (Z. Li).

<https://doi.org/10.1016/j.apcatb.2019.01.073>

Received 21 November 2018; Received in revised form 20 January 2019; Accepted 27 January 2019

Available online 29 January 2019

0926-3373/© 2019 Elsevier B.V. All rights reserved.

can serve as the active site in MoS<sub>2</sub> nanodots [35]. Therefore, MoS<sub>2</sub> quantum dots (QDs) appears to be a more favorable candidate as the co-catalyst for photocatalytic hydrogen evolution.

In this work, We presented the construction and characterization of ternary g-C<sub>3</sub>N<sub>4</sub>/NCDS/MoS<sub>2</sub> QDs photocatalysts and their visible-light induced photocatalytic hydrogen evolution activity. The effects of NCDS and MoS<sub>2</sub> QDs contents on H<sub>2</sub> evolution rate of g-C<sub>3</sub>N<sub>4</sub>/NCDS/MoS<sub>2</sub> QDs were studied. The results indicated that both NCDS and MoS<sub>2</sub> were crucial to increasing the photocatalytic activity. The prepared ternary g-C<sub>3</sub>N<sub>4</sub>/NCDS/MoS<sub>2</sub> QDs composites showed remarkably enhanced photocatalytic H<sub>2</sub> evolution activities compared to g-C<sub>3</sub>N<sub>4</sub>/NCDS and g-C<sub>3</sub>N<sub>4</sub>/MoS<sub>2</sub>. Based on the experimental results, proper mechanisms were proposed to account for the improved photocatalytic H<sub>2</sub> evolution activity. To the best of our knowledge, the ternary g-C<sub>3</sub>N<sub>4</sub>/NCDS/MoS<sub>2</sub> photocatalyst has not been reported yet. Therefore, this work presents a novel photocatalyst system for the potential application in photocatalytic fields.

## 2. Experimental section

### 2.1. Sample preparation

#### 2.1.1. Materials

Dicyandiamide (C<sub>2</sub>H<sub>4</sub>N<sub>4</sub>, 99%), *N,N*-Dimethylformamide (DMF), Urea, Citric acid, Ammonium tetrathiomolybdate ((NH<sub>4</sub>)<sub>2</sub>MoS<sub>4</sub>), hydrochloric acid, were obtained from Aladdin Reagent Co., Ltd. All reagents were used without further purification.

#### 2.1.2. Preparation of bulk g-C<sub>3</sub>N<sub>4</sub>

The synthesis of bulk g-C<sub>3</sub>N<sub>4</sub> was based on a published method [36,37]. Typically, 5.0 g of dicyandiamide was introduced into an alumina crucible with a cover which was heated to 550 °C for 3 h with a heating rate of 3 °C/min. The obtained bulk g-C<sub>3</sub>N<sub>4</sub> was ground into powder.

#### 2.1.3. Preparation of NCDS and bulk g-C<sub>3</sub>N<sub>4</sub>/NCDS photocatalyst

N-doped carbon dots (NCDS) were synthesized via a hydrothermal method [36]. Detailed experimental process was listed in the supporting information. The preparation process of bulk g-C<sub>3</sub>N<sub>4</sub>/NCDS was as follows: a certain quantity of NCDS was dissolved in 20 mL of DI water. Then, 3.0 g of dicyandiamide was added into above solution. The mixture was mechanically stirred at 70 °C to remove the solvent. The obtained powder was subsequently heated to 550 °C for 3 h at a heating rate of 3 °C/min. After being cooled to room temperature, the resultant yellow powder was collected. The obtained sample was denoted as bulk g-C<sub>3</sub>N<sub>4</sub>/NCDS-x. x represented the mass fraction of NCDS contained in the composite. Different bulk g-C<sub>3</sub>N<sub>4</sub>/NCDS samples with NCDS at mass percentages of 1.0%, 1.5%, 2.0%, 2.5%, and 3.0% were prepared through the same procedure.

#### 2.1.4. Preparation of protonated g-C<sub>3</sub>N<sub>4</sub>/NCDS photocatalyst and protonated g-C<sub>3</sub>N<sub>4</sub>

1.0 g of bulk g-C<sub>3</sub>N<sub>4</sub>/NCDS-x was dispersed into 50 mL of 6 M HCl solution, the obtained mixture was transferred to a teflonlined stainless steel autoclave and heated to 130 °C for 5 h. After being cooled to room temperature, the photocatalyst was obtained by centrifugation-oscillation-ultrasonic cycle several times and vacuum drying at 80 °C for 5 h. The obtained photocatalyst was denoted as protonated g-C<sub>3</sub>N<sub>4</sub>/NCDS-x. Protonated g-C<sub>3</sub>N<sub>4</sub> was prepared in the same manner as protonated g-C<sub>3</sub>N<sub>4</sub>/NCDS except that bulk g-C<sub>3</sub>N<sub>4</sub>/NCDS-x was replaced with bulk g-C<sub>3</sub>N<sub>4</sub>.

#### 2.1.5. Preparation of g-C<sub>3</sub>N<sub>4</sub>/NCDS/MoS<sub>2</sub> and g-C<sub>3</sub>N<sub>4</sub>/MoS<sub>2</sub> photocatalyst

A quantity of (NH<sub>4</sub>)<sub>2</sub>MoS<sub>4</sub> was dissolved in *N,N*-dimethylformamide (DMF), 60 mg of protonated g-C<sub>3</sub>N<sub>4</sub>/NCDS-2.0% was mixed with the above solution, and then sonicated for 1 h. The above mixture was

transferred to a 100 mL Teflon-lined autoclave and treated at 200 °C for 24 h. The product was collected by centrifugation and washed several times with deionized water to completely remove DMF. The obtained product was dried at 70 °C overnight and denoted as g-C<sub>3</sub>N<sub>4</sub>/NCDS/MoS<sub>2</sub>-x, x represented the weight percentage of MoS<sub>2</sub> in the composite. g-C<sub>3</sub>N<sub>4</sub>/MoS<sub>2</sub> was prepared in the same manner as g-C<sub>3</sub>N<sub>4</sub>/NCDS/MoS<sub>2</sub> except that the protonated g-C<sub>3</sub>N<sub>4</sub>/NCDS was replaced with protonated g-C<sub>3</sub>N<sub>4</sub>.

### 2.2. Characterization techniques

Powder X-ray diffraction (XRD) patterns were obtained using an Empyrean multipurpose research diffractometer (Panalytical Empyrean XRD) with Cu K $\alpha$  radiation ( $\lambda = 1.5406 \text{ \AA}$ ). Transition electron microscopy (TEM) images were recored with a JEOL 2100 TEM microscope. X-ray photoelectron spectroscopy (XPS) and valence band XPS (VB XPS) were obtained by using Thermo Escalab 150 spectrometer with an Al K $\alpha$  X-ray. The fluorescence properties of the samples were measured using a Hitachi fluorescence spectrometer (model F-4600), which is the excitation source. Brunauer-Emmett-Teller (BET) surface area was obtained at 77 K on a Quantachrome specific surface and aperture meter (NOVA 1000e). UV–vis diffuse reflectance spectra (DRS) were constructed on an Agilent Cary 100 UV–vis spectrophotometer equipped. FTIR spectra were performed with a Nicolet Nexus 470 spectrometer.

### 2.3. Photocatalytic activity test

Photocatalytic hydrogen evolution activity was evaluated using CEL-SPH2N photolysis water production system (Beijing Zhongjiao Jinyuan Technology Co., Ltd). A self-made glass vessel was used as a photocatalytic reactor (reactor volume of 500 mL). Prior to performing the photocatalytic reaction, a vacuum pump was started to evacuate the reactor and the hydrogen circulation path. During the catalytic reaction, the reaction was maintained at a constant temperature with circulating condensed water, and the system was stirred with a magnetic stirrer to keep it in suspension. 0.05 g photocatalyst was dispersed in 100 mL of water containing 10 vol.% triethanolamine as a sacrificial agent. The suspension was evacuated several times to completely remove air. The light-irradiation was carried out by using a 300 W Xe-lamp (Profect Light, PLS-SXE300C) with a 420 nm cutoff filter as the visible light source. The generated H<sub>2</sub> was automatically analyzed every 1 h by a gas chromatographer (GC-7920) equipped with a thermal conductivity detector with high purity N<sub>2</sub> as a carrier gas.

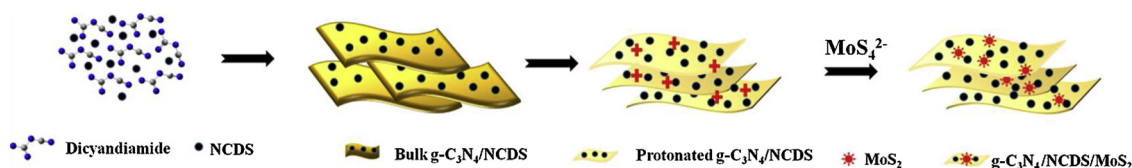
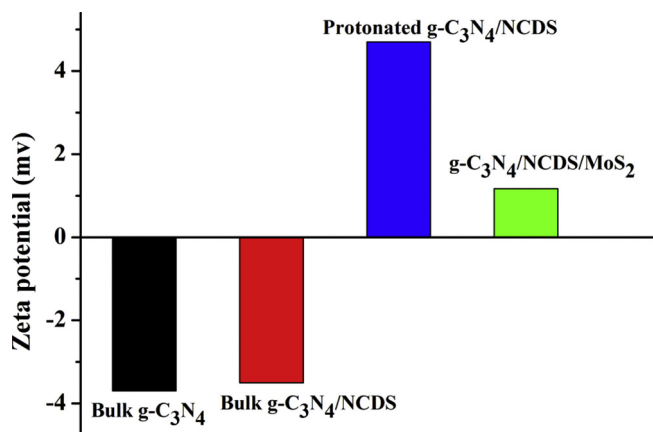
### 2.4. Photoelectrochemical measurement

Electrochemical test was conducted by using standard three-electrode system, where catalyst as working electrode, platinum plate electrode as counter electrode and Ag/AgCl as reference electrode. A Na<sub>2</sub>SO<sub>4</sub> solution (0.5 M) was used as the electrolyte, and the light source was a 300 W Xe lamp. The electrochemical impedance spectroscopy of the samples was tested by the AC Impedance mode of the RST 5200 electrochemical workstation. The instantaneous photocurrent test was performed by using the Amperometric i-t curve mode. Electrochemical impedance spectroscopy (EIS) was performed over a frequency range of 10<sup>3</sup> to 10<sup>5</sup> Hz with an AC voltage amplitude of 5 mV.

## 3. Results and discussion

### 3.1. The formation process of g-C<sub>3</sub>N<sub>4</sub>/NCDS/MoS<sub>2</sub>

The process for synthesizing the g-C<sub>3</sub>N<sub>4</sub>/NCDS/MoS<sub>2</sub> composite is schematically illustrated in Scheme 1. In order to investigate the formation process of g-C<sub>3</sub>N<sub>4</sub>/NCDS/MoS<sub>2</sub> composite materials, the surface charge of bulk g-C<sub>3</sub>N<sub>4</sub>, bulk g-C<sub>3</sub>N<sub>4</sub>/NCDS, protonated g-C<sub>3</sub>N<sub>4</sub>/NCDS

Scheme 1. Schematic illustration of the synthesis of the g-C<sub>3</sub>N<sub>4</sub>/NCDS/MoS<sub>2</sub>.Fig. 1. The zeta potentials of bulk g-C<sub>3</sub>N<sub>4</sub>, bulk g-C<sub>3</sub>N<sub>4</sub>/NCDS, protonated g-C<sub>3</sub>N<sub>4</sub>/NCDS, and g-C<sub>3</sub>N<sub>4</sub>/NCDS/MoS<sub>2</sub> photocatalysts.

and g-C<sub>3</sub>N<sub>4</sub>/NCDS/MoS<sub>2</sub> were measured and the results were given in Fig. 1. The Z-potential of bulk g-C<sub>3</sub>N<sub>4</sub> and bulk g-C<sub>3</sub>N<sub>4</sub>/NCDS was -3.7 mV and -3.5 mV, respectively, indicating that loading NCDS on bulk g-C<sub>3</sub>N<sub>4</sub> did not change the surface charge of bulk g-C<sub>3</sub>N<sub>4</sub>. The Z-potential of protonated g-C<sub>3</sub>N<sub>4</sub>/NCDS was 4.7 mV, which displayed that the protonation of g-C<sub>3</sub>N<sub>4</sub>/NCDS with hydrochloric acid converted the surface charge of g-C<sub>3</sub>N<sub>4</sub>/NCDS from negative to positive. Thus, self-assembly formation of g-C<sub>3</sub>N<sub>4</sub>/NCDS/MoS<sub>2</sub> was achieved by electrostatic adsorption between the negatively charged MoS<sub>4</sub><sup>2-</sup> and the positively charged g-C<sub>3</sub>N<sub>4</sub>/NCDS.

### 3.2. XRD analysis

XRD analysis was used to investigate the phase structure of the photocatalysts (Fig. 2a). The bulk g-C<sub>3</sub>N<sub>4</sub> had two obvious peaks at 13.1° and 27.7°. The lower angle diffraction peak at 13.1° was indexed as tri-s-triazine units (100) reflections, and the one centering at 27.7° could be indexed to the stacking of the conjugated double bonds for the interlayer stacking of aromatic segments (002) [38]. A typical diffraction peak of bulk g-C<sub>3</sub>N<sub>4</sub> could be observed in protonated g-C<sub>3</sub>N<sub>4</sub>, which meant that g-C<sub>3</sub>N<sub>4</sub> with a graphite-like layer structure was not changed after protonation. Somewhat differently, the intensity of the (002) peak

of protonated g-C<sub>3</sub>N<sub>4</sub> was lower than that of bulk g-C<sub>3</sub>N<sub>4</sub>, together with a shift in the (002) peak location from 27.4° for bulk g-C<sub>3</sub>N<sub>4</sub> to 27.6° for g-C<sub>3</sub>N<sub>4</sub>/NCDS/MoS<sub>2</sub>-3% (Fig. 2b), describing a few-layered structure of protonated g-C<sub>3</sub>N<sub>4</sub>. In addition, due to the low quantity of MoS<sub>2</sub> dispersed on the g-C<sub>3</sub>N<sub>4</sub>, no significant peak of MoS<sub>2</sub> was found in the g-C<sub>3</sub>N<sub>4</sub>/NCDS/MoS<sub>2</sub>-3% composite.

### 3.3. TEM analysis

The morphology and microstructure of the samples were investigated by TEM and HRTEM (Fig. 3). The TEM image in Fig. 3a–b displayed the spherical morphology of NCDS and MoS<sub>2</sub> QDs without obvious aggregation. TEM images of the g-C<sub>3</sub>N<sub>4</sub>/NCDS/MoS<sub>2</sub>-3% composite samples (Fig. 3c) showed that the thin and flaked g-C<sub>3</sub>N<sub>4</sub> was modified with randomly distributed crystalline NCDS and MoS<sub>2</sub> QDs. As shown in Fig. 3d, the crystalline lattice distance of 0.53 nm could be corresponded to the (002) plane of MoS<sub>2</sub>, the lattice spacing of 0.27 nm corresponded to NCDS and the lattice spacing of 0.36 nm corresponded to the (002) plane of g-C<sub>3</sub>N<sub>4</sub>. In addition, the HAADF-STEM element mapping of g-C<sub>3</sub>N<sub>4</sub>/NCDS/MoS<sub>2</sub>-3% samples (Fig. 3e) further demonstrated that MoS<sub>2</sub> QDs were well dispersed on g-C<sub>3</sub>N<sub>4</sub> nanosheet. The result showed that all the major elements of C, N, Mo, and S were uniformly distributed in the structure of g-C<sub>3</sub>N<sub>4</sub>/NCDS/MoS<sub>2</sub>-3% sample, which further confirmed that MoS<sub>2</sub> QDs were deposited on the surface of g-C<sub>3</sub>N<sub>4</sub>.

### 3.4. XPS analysis

XPS was used to analysis the elemental composition and chemical states of g-C<sub>3</sub>N<sub>4</sub>/NCDS/MoS<sub>2</sub>-3% sample (Fig. 4a, b, c, d). Fig.S1 presented the XPS survey spectrum of the composite, including elements of C, N, O and also a small amount of Mo and S. Typical peaks could be detected at binding energies of 289.8 (C 1s), 401.4 (N 1s), 537.6 (O 1s), 226.4 (Mo 3d). The C 1s peak in Fig. 4a could be deconvoluted into two peaks at 288.1 eV and 284.6 eV. The strong one at 284.5 eV was corresponding to sp<sup>2</sup> carbon bonded to the three nitrogen atoms in the carbon nitride lattice [39–41], and the weak one represented the surface adventitious carbon [42,43]. N 1s in Fig. 4b had four asymmetrical peaks at 395.0, 396.5, 397.6 and 401.0 eV, respectively, which could be attributed to C–N=C sp<sup>2</sup>–bonded N atoms in graphite-like g-C<sub>3</sub>N<sub>4</sub> structure, tertiary (N–(C)3) groups, amino functional groups

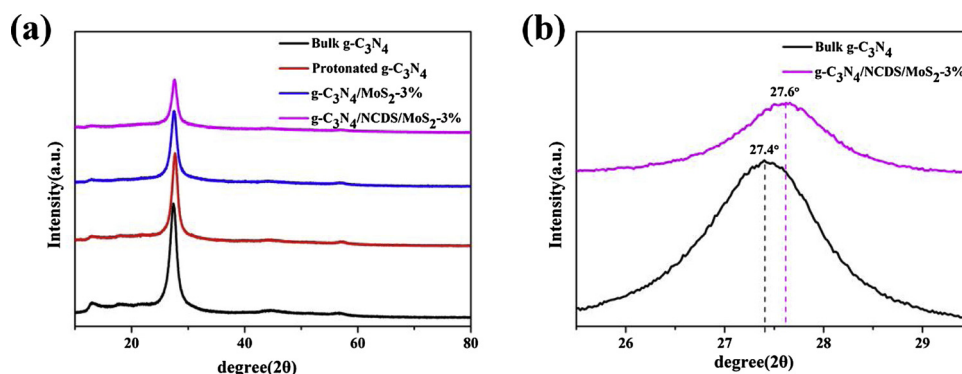
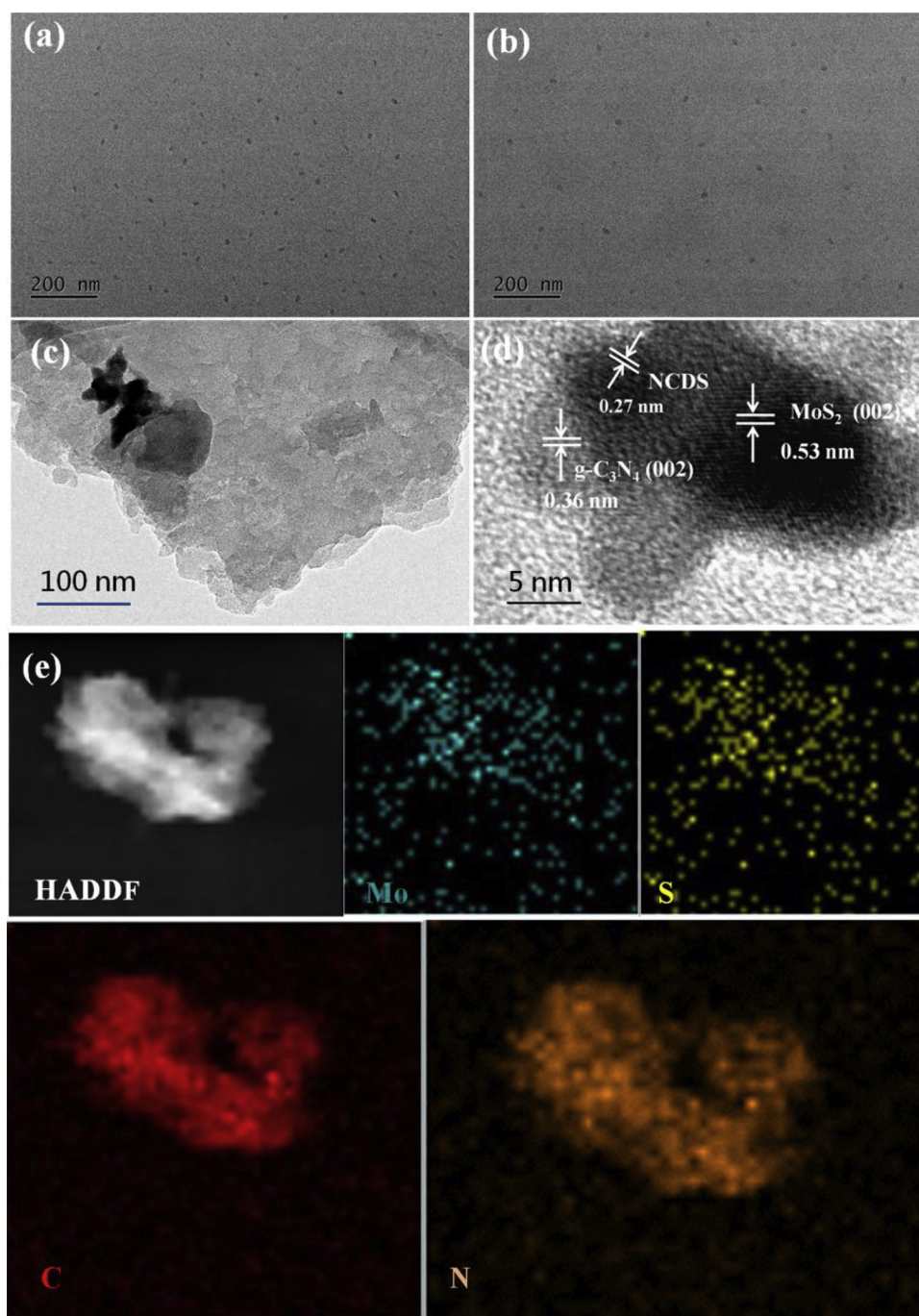


Fig. 2. XRD patterns of samples.





**Fig. 3.** TEM and HRTEM images of (a) NCDS and (b) MoS<sub>2</sub> QDs; (c–d) g-C<sub>3</sub>N<sub>4</sub>/NCDS/MoS<sub>2</sub>-3%; (e) STEM-EDX image of g-C<sub>3</sub>N<sub>4</sub>/NCDS/MoS<sub>2</sub>-3% composite and the corresponding element mapping for C, N, Mo, and S.

(C–N–H), and charging effect in heptazine rings [44–46]. Fig. 4c showed the Mo 3d XPS spectrum. The Mo 3d peaks (Fig. 3c) located at 228.7 and 231.7 eV were attributed to Mo 3d<sub>5/2</sub> and Mo 3d<sub>3/2</sub>, respectively. The S 2p spectrum in Fig. 4d presented two obvious peaks at 160.90 and 164.70 eV, corresponding to the S 2p<sub>3/2</sub> and S 2p<sub>1/2</sub>, respectively, demonstrating the existence of S<sup>2−</sup> state in the photocatalyst [47,48]. The XPS results showed that the MoS<sub>2</sub> had been successfully deposited onto the g-C<sub>3</sub>N<sub>4</sub> nanosheet surface.

### 3.5. BET surface areas and pore size distributions

The nitrogen adsorption desorption isotherms and pore size distribution curves of bulk g-C<sub>3</sub>N<sub>4</sub>, g-C<sub>3</sub>N<sub>4</sub>/MoS<sub>2</sub>-3% and g-C<sub>3</sub>N<sub>4</sub>/NCDS/

MoS<sub>2</sub>-3% composite photocatalysts were shown in Fig. 5. The type of adsorption-desorption isotherms for all samples shown in Fig. 5a belonged to Type IV, indicating that the carbon nitride materials belonged to the mesoporous material. The specific surface area and pore size of bulk g-C<sub>3</sub>N<sub>4</sub>, g-C<sub>3</sub>N<sub>4</sub>/MoS<sub>2</sub>-3% and g-C<sub>3</sub>N<sub>4</sub>/NCDS/MoS<sub>2</sub>-3% are listed in Table 1. The specific surface area of g-C<sub>3</sub>N<sub>4</sub>/NCDS/MoS<sub>2</sub>-3% was 71.39 m<sup>2</sup>/g, which was higher than that of bulk g-C<sub>3</sub>N<sub>4</sub> (25.18 m<sup>2</sup>/g) and g-C<sub>3</sub>N<sub>4</sub>/MoS<sub>2</sub>-3% (57.04 m<sup>2</sup>/g). The increased surface area could be attributed to the exfoliation of bulk g-C<sub>3</sub>N<sub>4</sub> in the process of protonation and the loading of MoS<sub>2</sub>, which facilitate the increase of active sites and thus enhancing the photocatalytic hydrogen evolution activity. From Table 1, it was found that the pore volume of g-C<sub>3</sub>N<sub>4</sub>/NCDS/MoS<sub>2</sub>-3% and g-C<sub>3</sub>N<sub>4</sub>/MoS<sub>2</sub>-3% was also increased.

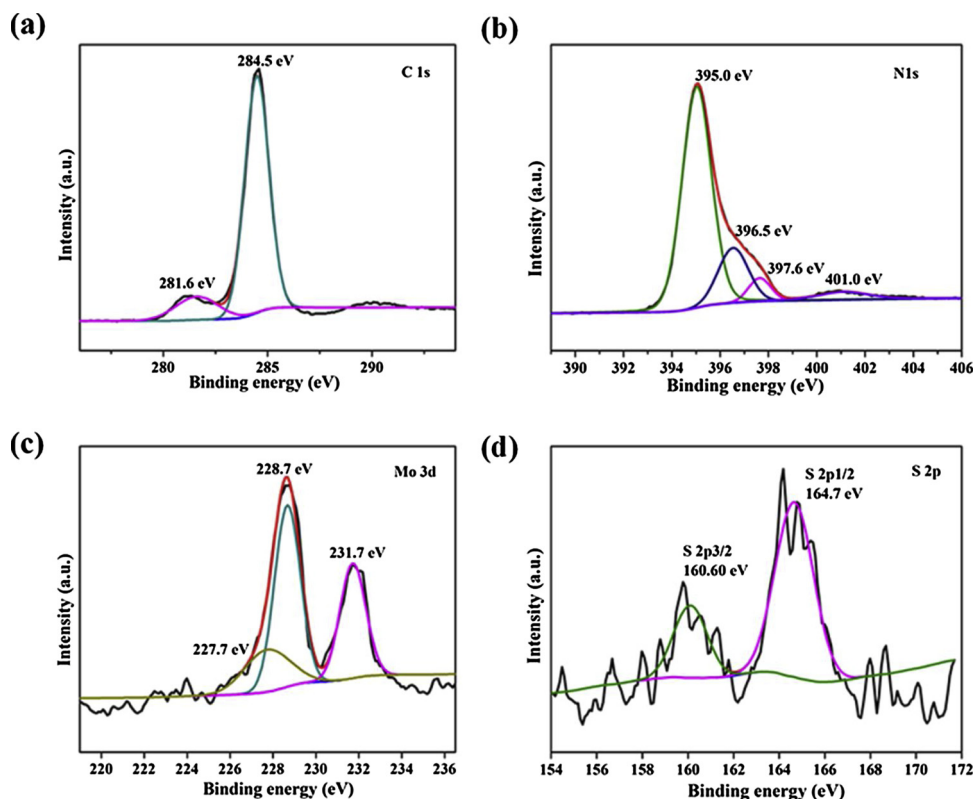


Fig. 4. The XPS spectra of g-C<sub>3</sub>N<sub>4</sub>/NCDS/MoS<sub>2</sub>-3% composite: (a) C 1 s, (b) N 1 s, (c) Mo 3d, and (d) S 2p.

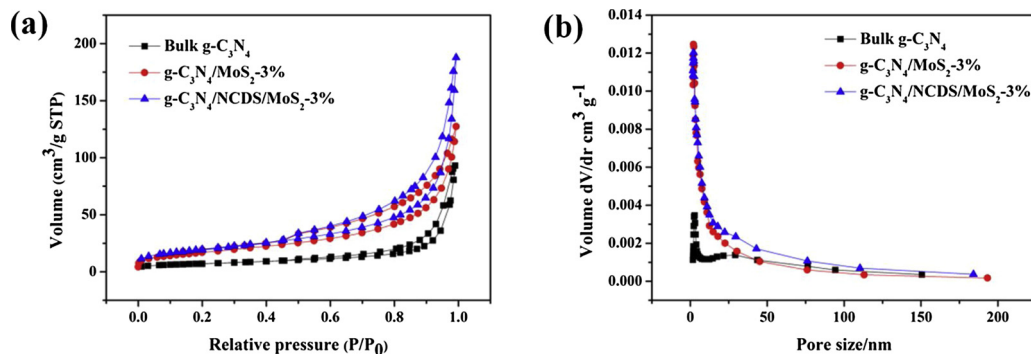


Fig. 5. (a) Nitrogen adsorption-desorption curve and (b) Pore size distribution curve of bulk g-C<sub>3</sub>N<sub>4</sub>, g-C<sub>3</sub>N<sub>4</sub>/MoS<sub>2</sub>-3% and g-C<sub>3</sub>N<sub>4</sub>/NCDS/MoS<sub>2</sub>-3% complexes.

**Table 1**

Summary of specific surface area and pore size of bulk g-C<sub>3</sub>N<sub>4</sub> and g-C<sub>3</sub>N<sub>4</sub>/NCDS/MoS<sub>2</sub>-3%.

Sample	Specific surface area (m <sup>2</sup> /g)	Pore volume (mL/g)
Bulk g-C <sub>3</sub> N <sub>4</sub>	25.18	0.004
g-C <sub>3</sub> N <sub>4</sub> /MoS <sub>2</sub> -3%	57.04	0.014
g-C <sub>3</sub> N <sub>4</sub> /NCDS/MoS <sub>2</sub> -3%	71.39	0.012

### 3.6. UV-vis DRS analysis

The optical properties of bulk g-C<sub>3</sub>N<sub>4</sub>, protonated g-C<sub>3</sub>N<sub>4</sub>, g-C<sub>3</sub>N<sub>4</sub>/MoS<sub>2</sub>-3% and g-C<sub>3</sub>N<sub>4</sub>/NCDS/MoS<sub>2</sub> with different MoS<sub>2</sub> quantities were recorded in Fig. 6a. In comparison with pure g-C<sub>3</sub>N<sub>4</sub>, a broader absorption in the visible region was observed for the g-C<sub>3</sub>N<sub>4</sub>/NCDS/MoS<sub>2</sub>-3% composite. Obviously, the absorption intensity for g-C<sub>3</sub>N<sub>4</sub>/NCDS/MoS<sub>2</sub>-3% in the visible region was strengthened as the content of MoS<sub>2</sub> increased due to the intrinsic absorption of black-colored MoS<sub>2</sub> nanoparticles. Compared with the protonated g-C<sub>3</sub>N<sub>4</sub>, the g-C<sub>3</sub>N<sub>4</sub>/NCDS/MoS<sub>2</sub>-3% sample showed enhanced absorption of the visible-light in the

range of 440–800 nm, which covered a large part of the visible spectrum. The enhanced visible-light adsorption ability of the composite could improve the light utilization to generate more available photo-generated electrons for participating in the photocatalytic reaction towards H<sub>2</sub> evolution. The plots of  $(\alpha h\nu)^2$  versus band-gap energy ( $h\nu$ ) of g-C<sub>3</sub>N<sub>4</sub> samples was given in Fig. 6b. Compared with the bandgap of bulk g-C<sub>3</sub>N<sub>4</sub> (2.82 eV), protonated g-C<sub>3</sub>N<sub>4</sub> had a larger bandgap (2.88 eV), the reason for which was attributed to the well-known quantum confinement effect. The conduction band and valence band potential of g-C<sub>3</sub>N<sub>4</sub> could be calculated by Eqs. (1) and (2) [49].

$$E_{VB} = \chi - E_e + 0.5E_g \quad (1)$$

$$E_{CB} = E_{VB} - E_g \quad (2)$$

Among them,  $\chi$  represents the electronegativity of the semiconductor. According to the literature, the electronegativity of g-C<sub>3</sub>N<sub>4</sub> is 4.72 eV [50], and the  $E_e$  value is 4.5 eV (vs NHE). Calculated by the above formula, the g-C<sub>3</sub>N<sub>4</sub> nanosheet had a valence band potential of 1.62 eV and a conduction band potential of −1.21 eV.

Fig. S2 (a) and Fig. S2 (b) showed band-gap energy ( $h\nu$ ) and

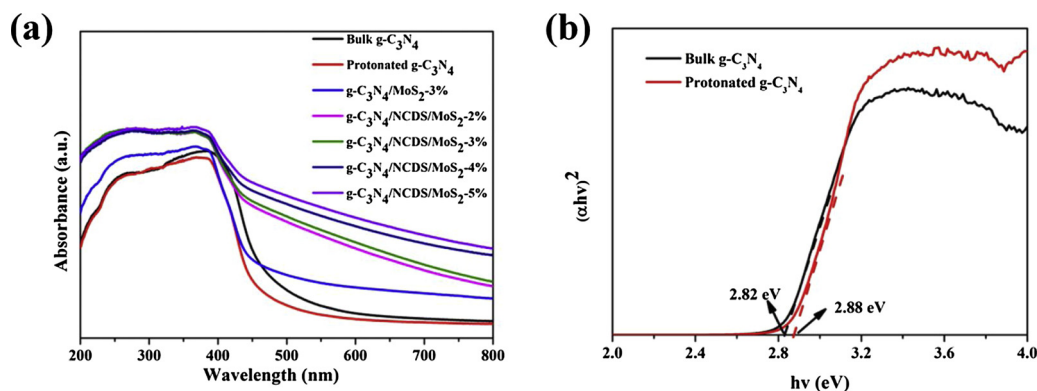


Fig. 6. (a) UV-vis diffuse reflectance spectra and (b) the plots of  $(\alpha h\nu)^2$  versus band-gap energy ( $h\nu$ ) of bulk g-C<sub>3</sub>N<sub>4</sub> and g-C<sub>3</sub>N<sub>4</sub> nanosheet samples.

Valence-band XPS spectra of NCDS, respectively. The corresponding CB and VB positions of NCDS was calculated based on Eq. (2) were 0.57 eV and 1.87 eV, respectively.

### 3.7. FT-IR analysis

The chemical functional groups of the sample were studied by FTIR spectra given in Fig. 7. The absorption band at about 808 cm<sup>-1</sup> corresponded to the breathing mode of the triazine-units. The bands in the region of 1000–1700 cm<sup>-1</sup> were derived from the aromatic C–N stretching [51,52], the wider band at 3430 cm<sup>-1</sup> was attributed to C–OH and N–H stretching vibrations [53]. Both pure g-C<sub>3</sub>N<sub>4</sub> and g-C<sub>3</sub>N<sub>4</sub>/NCDS/MoS<sub>2</sub>-3% had similar absorption bands, which demonstrated that the introduction of NCDS and MoS<sub>2</sub> did not change the g-C<sub>3</sub>N<sub>4</sub> layer structure. No MoS<sub>2</sub> peak was detected according to the IR spectra. These results were in well consistent with the XRD analysis.

### 3.8. Photocatalytic activity and stability

The photocatalytic hydrogen evolution performance of as-prepared photocatalysts was summarized in Fig. 8. When no co-catalyst was deposited on the surface of bulk g-C<sub>3</sub>N<sub>4</sub> and protonated g-C<sub>3</sub>N<sub>4</sub>/NCDS, both of them had almost no hydrogen evolution performance. After introducing co-catalyst of MoS<sub>2</sub>, protonated g-C<sub>3</sub>N<sub>4</sub> (g-C<sub>3</sub>N<sub>4</sub>/MoS<sub>2</sub>-3%) exhibited a rather low photocatalytic activity with an average H<sub>2</sub> evolution rate of 4.03 μmol g<sup>-1</sup> h<sup>-1</sup>, while the hydrogen evolution activity of g-C<sub>3</sub>N<sub>4</sub>/NCDS/MoS<sub>2</sub> can be significantly improved after the incorporation with NCDS. In order to find the optimum content of NCDS, 3% MoS<sub>2</sub> was deposited on the surface of protonated g-C<sub>3</sub>N<sub>4</sub>/NCDS for

photocatalytic hydrogen evolution performance test (Fig. 8a). The results showed that with the increase of NCDS content, the hydrogen evolution increased gradually. When the content of NCDS reached 2.0%, the hydrogen evolution performance reached optimal. After that, the content of NCDS continued to increase, but the amount of hydrogen evolution decreased. The reason for the decrease could be ascribed to the shielding effect that the excessive black NCDS would partially block the light absorption of g-C<sub>3</sub>N<sub>4</sub>.

In addition to NCDS, MoS<sub>2</sub> loading had a greater impact on the hydrogen evolution activity of the composite system (Fig. 8b). With the increase of MoS<sub>2</sub> loading, the hydrogen evolution activity of the composite system was increased. When the loading of MoS<sub>2</sub> was 3 wt%, the composites g-C<sub>3</sub>N<sub>4</sub>/NCDS/MoS<sub>2</sub>-3% had the highest photocatalytic performance. The rate of hydrogen evolution was 212.41 μmol g<sup>-1</sup> h<sup>-1</sup>, which was 53 times higher than that of g-C<sub>3</sub>N<sub>4</sub>/MoS<sub>2</sub>-3%. Further increasing the load of MoS<sub>2</sub>, the hydrogen evolution activity of g-C<sub>3</sub>N<sub>4</sub>/NCDS/MoS<sub>2</sub> gradually decreased. The reason for the decrease in hydrogen evolution activity may be related to the following two aspects: first, excessive MoS<sub>2</sub> nanoparticles loaded on the protonated g-C<sub>3</sub>N<sub>4</sub>/NCDS will have a hiding effect and hinder the absorption of light by the composite photocatalyst; second, overcharged MoS<sub>2</sub> will partially become the recombination center of photogenerated carriers, which can inhibit the hydrogen evolution activity of the catalyst. Therefore, the high or low MoS<sub>2</sub> loading was unfavorable for the photocatalytic hydrogen evolution activity of the composite system. The above results indicated that both NCDS and MoS<sub>2</sub> played important roles in the photocatalytic process. The rate of H<sub>2</sub> production of ternary composite photocatalysts prepared from melamine and urea were also tested, respectively. There is no significant difference in hydrogen production performance (Fig. S3).

The cycling stability of the photocatalyst was also an indispensable index for investigating its photocatalytic effect. To determine the photostability of g-C<sub>3</sub>N<sub>4</sub>/NCDS/MoS<sub>2</sub>-3%, the cycling stability of the g-C<sub>3</sub>N<sub>4</sub>/NCDS/MoS<sub>2</sub>-3% sample was investigated. The cycling photocatalytic test for g-C<sub>3</sub>N<sub>4</sub>/NCDS/MoS<sub>2</sub>-3% under intermittent visible light irradiation was conducted and illustrated in Fig. 9. It was clear that, for four consecutive cycling photocatalytic experiments, the photocatalytic hydrogen evolution activity of g-C<sub>3</sub>N<sub>4</sub>/NCDS/MoS<sub>2</sub>-3% remained stable without obvious decreasing.

### 3.9. Charge transfer and separation

PL analysis was further studied the charge separation and transfer ability of the obtained bulk g-C<sub>3</sub>N<sub>4</sub>, protonated g-C<sub>3</sub>N<sub>4</sub>, g-C<sub>3</sub>N<sub>4</sub>/MoS<sub>2</sub>-3% and g-C<sub>3</sub>N<sub>4</sub>/NCDS/MoS<sub>2</sub>-3% sample, the result was displayed in Fig. 10. All the samples exhibited broad PL peak centered at 460 nm under the 370 nm excitation at room temperature. Comparing all the spectra, it could be observed that PL intensity obviously decreases with the introduction of MoS<sub>2</sub> and NCDS. When 3 wt % MoS<sub>2</sub> was loaded on

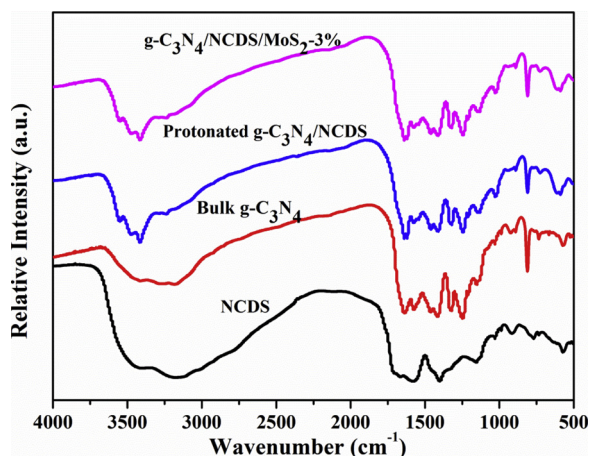
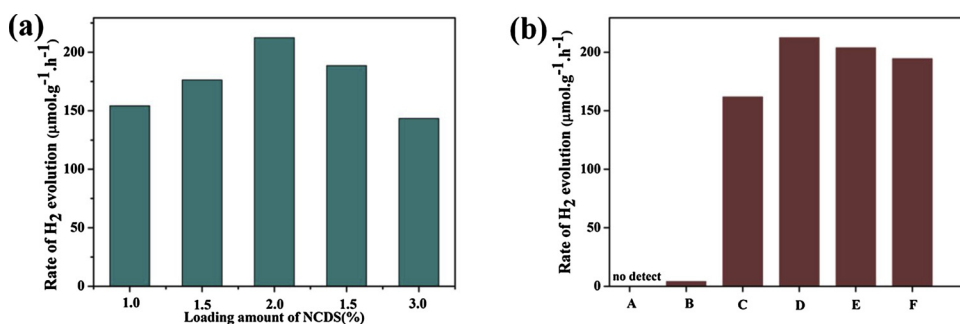
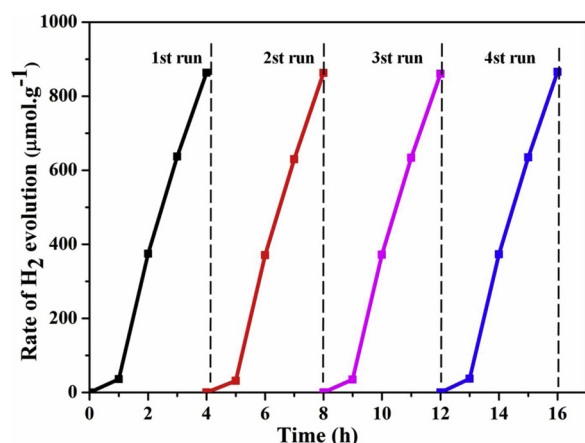


Fig. 7. FT-IR spectra of NCDS, bulk g-C<sub>3</sub>N<sub>4</sub>, protonated g-C<sub>3</sub>N<sub>4</sub>/NCDS, and g-C<sub>3</sub>N<sub>4</sub>/NCDS/MoS<sub>2</sub>-3%.





**Fig. 8.** (a) The rate of  $H_2$  production over  $g-C_3N_4/NCDS/MoS_2$  photocatalysts loaded with 3%  $MoS_2$  and various amounts of NCDS under visible light irradiation ( $\lambda > 420$  nm). (b) Photocatalytic reaction of  $g-C_3N_4/NCDS/MoS_2$  composite photocatalyst in visible Light ( $\lambda \geq 420$  nm) for 3 h. (A: bulk  $g-C_3N_4$ . B:  $g-C_3N_4/MoS_2$ -3%. C:  $g-C_3N_4/NCDS/MoS_2$ -2%. D:  $g-C_3N_4/NCDS/MoS_2$ -3%. E:  $g-C_3N_4/NCDS/MoS_2$ -4%. F:  $g-C_3N_4/NCDS/MoS_2$ -5%).



**Fig. 9.** Photocatalytic hydrogen production over ( $g-C_3N_4/NCDS/MoS_2$ -3%) during 16 h, with evacuation every 4 h.

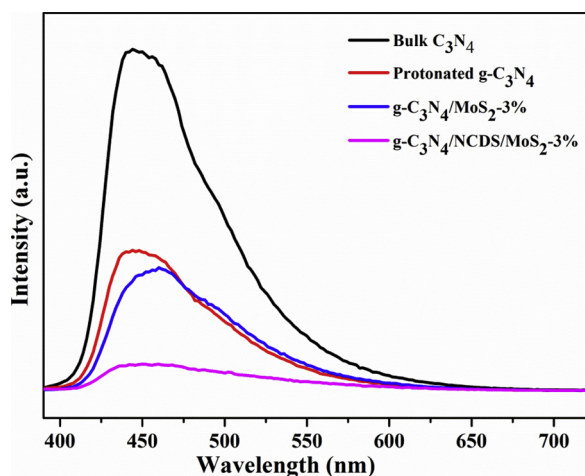


**Fig. 10.** The PL spectra of the as-prepared samples.

the surface of the  $g-C_3N_4/NCDS$ , the peak intensities drop obviously compared with those of the bulk  $C_3N_4$  and protonated  $g-C_3N_4$ , demonstrating that the combination of the photoinduced charge carriers was efficiently inhibited by the efficient interfacial charge transfer between the  $g-C_3N_4/NCDS$  and  $MoS_2$ .

The photogenerated charge separation and electron transfer performance of the  $g-C_3N_4/NCDS/MoS_2$  system were also studied using electrochemical impedance spectroscopy (EIS) and photocurrent responses. All samples exhibited a rapid and reproducible photocurrent response at each exposure (Fig. 11a). It was clear that the  $g-C_3N_4/NCDS/MoS_2$ -3% had a higher photocurrent density than that of bulk  $g-C_3N_4$ , which could be ascribed to the existence of  $MoS_2$  and NCDS, where photogenerated electrons and holes could be efficiently separated in space and the photogenerated carrier recombination would be

reduced, which kept consistent with the results of PL spectra shown in Fig. 10. As a result, the  $g-C_3N_4/NCDS/MoS_2$ -3% sample showed enhanced photocurrent. The improved transfer efficiency of charge carriers could lead to the enhanced photocatalytic activity of  $g-C_3N_4/NCDS/MoS_2$  photocatalysts. Electrochemical impedance spectroscopy (EIS) of bulk  $g-C_3N_4$ ,  $g-C_3N_4/MoS_2$ -3%, and  $g-C_3N_4/NCDS/MoS_2$ -3% samples was carried out to further investigate charge transfer and recombination processes in the  $g-C_3N_4/NCDS/MoS_2$  composites under the visible light irradiation, and the result was shown in Fig. 11b. Compared with bulk  $g-C_3N_4$  and  $g-C_3N_4/MoS_2$ -3%, the smaller arc radius on the EIS Nyquist plot of  $g-C_3N_4/NCDS/MoS_2$ -3% was observed, which indicated a more effective separation of photogenerated electron-hole pairs and a faster interfacial charge transfer had occurred on the surface. The EIS results were consistent with the photocurrents analysis, which further confirmed that the presence of NCDS and  $MoS_2$  was beneficial to separation of electron-hole pairs, thus leading to improved photocatalytic activities.

### 3.10. Photocatalytic mechanism

Based on all the above results, a proposed mechanism for the photocatalytic  $H_2$  evolution of  $g-C_3N_4/NCDS/MoS_2$  photocatalyst was illustrated in Fig. 12. Compared to the CB and VB positions of  $g-C_3N_4$  nanosheet and NCDS, it could be seen that the  $E_{CB}$  of  $g-C_3N_4$  nanosheet was more negative than that of NCDS and the  $E_{VB}$  of NCDS was more positive than that of  $g-C_3N_4$  nanosheet, as shown in Fig. 12a. It seemed that coupling  $g-C_3N_4$  nanosheet with NCDS will be form a type-II heterojunction. In this case, photogenerated electrons in the CB of  $g-C_3N_4$  would transfer to NCDS, whereas photogenerated holes in the VB of NCDS would transfer to  $g-C_3N_4$ . However, the accumulated electrons in the CB of NCDS could not reduce water into  $H_2$  because the  $E_{CB}$  of NCDS was more positive than the  $H^+/H_2$  redox potential, which was consistent with the fact that  $g-C_3N_4/NCDS$  had almost no hydrogen evolution performance. Thus, the photocatalytic  $H_2$  evolution activity of  $g-C_3N_4/NCDS/MoS_2$  will be closer to that of  $g-C_3N_4/MoS_2$ . Actually, the  $g-C_3N_4/NCDS/MoS_2$  composite showed highly efficient photocatalytic activities in comparison with  $g-C_3N_4/MoS_2$ . Therefore, the enhanced photocatalytic performance should be attributed to the formation of the Z-scheme charge transfer mode (Fig. 12b), which could effectively accelerate the transfer and separation of photogenerated charge carriers. Under visible light irradiation, both  $g-C_3N_4$  and NCDS could be easily excited to yield photogenerated electron-hole pairs. the photogenerated electrons from CB of NCDS would combine rapidly with the photogenerated holes from VB of  $g-C_3N_4$  nanosheet in the solid-solid interface owing to the short electron-migration distance between NCDS and  $g-C_3N_4$  nanosheet. So, the rich electrons on the CB of  $g-C_3N_4$  were further transmitted to the conduction band of  $MoS_2$ . The CB position of  $MoS_2$  located at  $-0.24$  eV [24]. Therefore, compared to  $MoS_2$ , the more negative CB level of  $g-C_3N_4$  facilitated to provide ample thermodynamic driving force for the photogenerated electrons transfer from the CB of  $g-C_3N_4$  to that of  $MoS_2$ , which also helps to promote the electrons transfer. More importantly, it was revealed that the unsaturated active S atoms on exposed edges of  $MoS_2$  could act as the

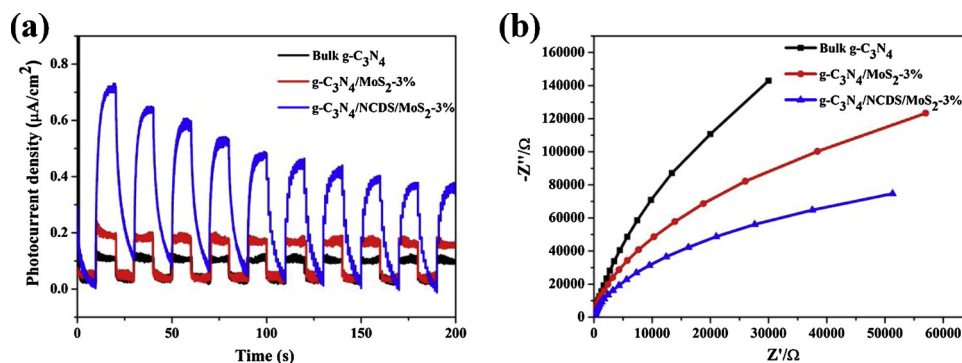


Fig. 11. Transient photocurrent density versus time plotted (a) and (b) EIS Nyquist plots of bulk g-C<sub>3</sub>N<sub>4</sub>, g-C<sub>3</sub>N<sub>4</sub>/MoS<sub>2</sub>-3%, and g-C<sub>3</sub>N<sub>4</sub>/NCDS/MoS<sub>2</sub>-3% under visible light ( $\lambda > 400$  nm) in 0.5 M Na<sub>2</sub>SO<sub>4</sub> electrolyte.

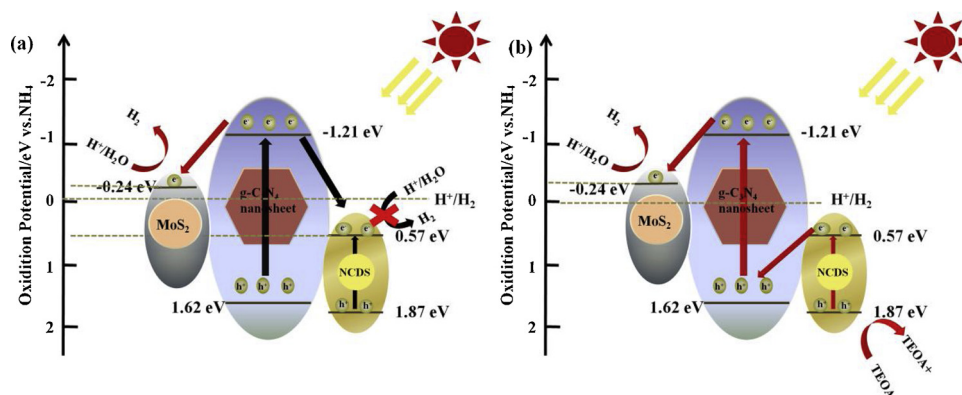


Fig. 12. Proposed photocatalytic mechanism for hydrogen evolution over g-C<sub>3</sub>N<sub>4</sub>/NCDS/MoS<sub>2</sub> under visible light irradiation.

active sites to promote the dissociation of water and the evolution of H<sub>2</sub>. The photogenerated holes in valence band of NCDS were quickly quenched by TEOA sacrificial agent. As a result, the synergistic effects of Z-scheme charge transfer mode and sufficient active sites for H<sub>2</sub> evolution resulted in the enhanced photocatalytic H<sub>2</sub> evolution activity of g-C<sub>3</sub>N<sub>4</sub>/NCDS/MoS<sub>2</sub> composite.

#### 4. Conclusion

In summary, the g-C<sub>3</sub>N<sub>4</sub>/NCDS/MoS<sub>2</sub> composites had been successfully prepared via an electrostatic self-assembly process followed by a solvothermal process. The protonation of g-C<sub>3</sub>N<sub>4</sub>/NCDS not only achieved the transformation of g-C<sub>3</sub>N<sub>4</sub>/NCDS from negative charge to positive charge, facilitating the electrostatic self-assembly, but also realized simultaneously the exfoliation of bulk g-C<sub>3</sub>N<sub>4</sub>/NCDS, which increased the surface area of composites and provided more active sites for H<sub>2</sub> evolution reaction. Ternary g-C<sub>3</sub>N<sub>4</sub>/NCDS/MoS<sub>2</sub> exhibited enhanced photocatalytic hydrogen evolution performance compared with the corresponding two-component systems such as g-C<sub>3</sub>N<sub>4</sub>/NCDS, g-C<sub>3</sub>N<sub>4</sub>/MoS<sub>2</sub>. The improvement of photocatalytic activities are attributed to the Z-scheme heterojunction formation between g-C<sub>3</sub>N<sub>4</sub> and NCDS, which facilitates the separation and transport of photogenerated charge carriers, enhancing the photocatalytic activity. Current work provided a new strategy for the design and synthesis of high performance composite photocatalysts for water splitting.

#### Acknowledgement

We gratefully acknowledge the support of this research by the National Natural Science Foundation of China (Nos. 21671176 and 21001096).

#### Appendix A. Supplementary data

Supplementary material related to this article can be found, in the online version, at doi:<https://doi.org/10.1016/j.apcatb.2019.01.073>.

#### References

- [1] X. Wang, K. Maeda, A. Thomas, K. Takanabe, G. Xin, J.M. Carlsson, K. Domen, M. Antonietti, *Nat. Mater.* 8 (2009) 76–80.
- [2] Y. Wang, S. Zhao, Y. Zhang, J. Fang, Y. Zhou, S. Yuan, C. Zhang, W. Chen, *Appl. Surf. Sci.* 440 (2018) 258–265.
- [3] J. Feng, D. Zhang, H. Zhou, M. Pi, X. Wang, S. Chen, *ACS Sustain. Chem. Eng.* 6 (2018) 6342–6349.
- [4] W. Che, W. Cheng, T. Yao, F. Tang, W. Liu, H. Su, Y. Huang, Q. Liu, J. Liu, F. Hu, Z. Pan, Z. Sun, S. Wei, *J. Am. Chem. Soc.* 139 (2017) 3021–3026.
- [5] Y. Shi, J. Chen, Z. Mao, B.D. Fahlman, D. Wang, *J. Catal.* 356 (2017) 22–31.
- [6] J. Zhang, Y. Hu, X. Jiang, S. Chen, S. Meng, X. Fu, *J. Hazard. Mater.* 280 (2014) 713–722.
- [7] L. Jiang, X. Yuan, Y. Pan, J. Liang, G. Zeng, Z. Wu, H. Wang, *Appl. Catal. B: Environ.* 217 (2017) 388–406.
- [8] L. Jiang, X. Yuan, G. Zeng, J. Liang, Z. Wu, H. Wang, *Environ. Sci.-Nano* 5 (2018) 599–615.
- [9] Y. Yang, S. Wang, Y. Li, J. Wang, L. Wang, *Chem. Asian J.* 12 (2017) 1421–1434.
- [10] G. Zhou, Y. Shan, Y.Y. Hu, X.Y. Xu, L.Y. Long, J.L. Zhang, J. Dai, J.H. Guo, J.C. Shen, S. Li, L.Z. Liu, X.L. Wu, *Nat. Commun.* 9 (2018) 3366.
- [11] Z. Lu, L. Zeng, W. Song, Z. Qin, D. Zeng, C. Xie, *Appl. Catal. B: Environ.* 202 (2017) 489–499.
- [12] Y. Bao, K. Chen, *Appl. Surf. Sci.* 437 (2018) 51–61.
- [13] X. Hao, J. Zhou, Z. Cui, Y. Wang, Y. Wang, Z. Zou, *Appl. Catal. B: Environ.* 229 (2018) 41–51.
- [14] H. Zhao, P. Jiang, W. Cai, *Chem. Asian J.* 12 (2017) 361–365.
- [15] Z. Xing, Z. Chen, X. Zong, L. Wang, *Chem. Commun.* 50 (2014) 6762–6764.
- [16] J. Liu, Y. Liu, N. Liu, Y. Han, X. Zhang, H. Huang, Y. Lifshitz, S.T. Lee, J. Zhong, Z. Kang, *Science* 346 (2015) 970–974.
- [17] F. Wang, P. Chen, Y. Feng, Z. Xie, Y. Liu, Y. Su, Q. Zhang, Y. Wang, K. Yao, W. Lv, G. Liu, *Appl. Catal. B: Environ.* 207 (2017) 103–113.
- [18] K. Sridharan, E. Jang, J.H. Park, J.H. Kim, J.H. Lee, T.J. Park, *Chem.-Eur. J.* 21 (2015) 9126–9132.
- [19] Y. Li, Z. Wang, T. Xia, H. Ju, K. Zhang, R. Long, Q. Xu, C. Wang, L. Song, J. Zhu, *Adv. Mater.* 28 (2016) 6959–6965.



- [20] X. Li, W. Bi, L. Zhang, S. Tao, W. Chu, Q. Zhang, Y. Luo, C. Wu, Y. Xie, *Adv. Mater.* 28 (2016) 2427–2431.
- [21] H. Yu, R. Shi, Y. Zhao, G.I. Waterhouse, L.Z. Wu, C.H. Tung, T. Zhang, *Adv. Mater.* 28 (2016) 9454–9477.
- [22] Y.-N. Liu, C.-C. Shen, N. Jiang, Z.-W. Zhao, X. Zhou, S.-J. Zhao, A.-W. Xu, *ACS Catal.* 7 (2017) 8228–8234.
- [23] J. Jiang, J. Yu, S. Cao, *J. Colloid Interface Sci.* 461 (2016) 56–63.
- [24] Y. Hou, Z. Wen, S. Cui, X. Guo, J. Chen, *Adv. Mater.* 25 (2013) 6291–6297.
- [25] Y. Yang, H. Fei, G. Ruan, C. Xiang, J.M. Tour, *Adv. Mater.* 26 (2014) 8163–8168.
- [26] L.S. Byskov, J.K. Nørskov, B.S. Clausen, H. Topsøe, *J. Catal.* 187 (1999) 109–122.
- [27] Y. Li, L. Wang, T. Cai, S. Zhang, Y. Liu, Y. Song, X. Dong, L. Hu, *Chem. Eng. J.* 321 (2017) 366–374.
- [28] L. Wang, Q. Zhang, J. Zhu, X. Duan, Z. Xu, Y. Liu, H. Yang, B. Lu, *Energy Storage Mater.* 16 (2018) 37–45.
- [29] Y. Li, K. Yin, L. Wang, X. Lu, Y. Zhang, Y. Liu, D. Yan, Y. Song, S. Luo, *Appl. Catal. B Environ.* 239 (2018) 537–544.
- [30] L. Wang, X. Duan, G. Wang, C. Liu, S. Luo, S. Zhang, Y. Zeng, Y. Xu, Y. Liu, X. Duan, *Appl. Catal. B Environ.* 186 (2016) 88–96.
- [31] Y. Liu, H. Zhang, J. Ke, J. Zhang, W. Tian, X. Xu, X. Duan, H. Sun, M.O. Tade, S. Wang, *Appl. Catal. B Environ.* 228 (2018) 64–74.
- [32] Q.Z. Huang, Y. Xiong, Q. Zhang, H.C. Yao, Z.J. Li, *Appl. Catal. B Environ.* 209 (2017) 514–522.
- [33] H. Zhao, Y. Dong, P. Jiang, H. Miao, G. Wang, J. Zhang, *J. Mater. Chem. A* 3 (2015) 7375–7381.
- [34] L. Wang, X. Liu, J. Luo, X. Duan, J. Crittenden, C. Liu, S. Zhang, Y. Pei, Y. Zeng, X. Duan, *Angew. Chem. Int. Ed.* 56 (2017) 7610–7614.
- [35] X. Shi, M. Fujitsuka, S. Kim, T. Majima, *Small* 14 (2018) e1703277.
- [36] F. Wang, P. Chen, Y. Feng, Z. Xie, Y. Liu, Y. Su, Q. Zhang, Y. Wang, K. Yao, W. Lv, *Appl. Catal. B: Environ.* 207 (2017) 103–113.
- [37] C. Dong, Z. Ma, R. Qie, X. Guo, C. Li, R. Wang, Y. Shi, B. Dai, X. Jia, *Appl. Catal. B: Environ.* 217 (2017) 629–636.
- [38] W. Gao, M. Wang, C. Ran, L. Li, *Chem. Commun. (Camb)* 51 (2015) 1709–1712.
- [39] L. Ge, F. Zuo, J. Liu, Q. Ma, C. Wang, D. Sun, L. Bartels, P. Feng, *J. Mater. Chem.* 116 (2012) 13708–13714.
- [40] A. Thomas, A. Fischer, F. Goettmann, M. Antonietti, J.-O. Müller, R. Schlögl, J.M. Carlsson, *J. Mater. Chem.* 18 (2008) 4893.
- [41] V.N. Khabashesku, J.L.Z. And, J.L. Margrave, *Cheminform* 29 (2000) no–no.
- [42] S.C. Yan, Z.S. Li, Z.G. Zou, *Langmuir* 25 (2009) 10397–10401.
- [43] X. Jin, X. Fan, J. Tian, R. Cheng, M. Li, L. Zhang, *Rsc Adv.* 6 (2016) 52611–52619.
- [44] D. Jingjing, C. Sheng, J. Mietek, Q. Shi Zhang, *ACS Nano* 9 (2015) 931–940.
- [45] J. Wen, X. Li, H. Li, S. Ma, K. He, Y. Xu, Y. Fang, W. Liu, Q. Gao, *Appl. Surf. Sci.* 358 (2015) 204–212.
- [46] L. Shi, L. Liang, F. Wang, M. Liu, K. Chen, K. Sun, N. Zhang, J. Sun, *ACS Sustain. Chem. Eng.* 3 (2015) 81–89.
- [47] H. Lv, Y. Liu, H. Tang, P. Zhang, J. Wang, *Appl. Surf. Sci.* 425 (2017).
- [48] L.M. Yang, Z.L. Chen, D. Cui, X.B. Luo, B. Liang, L.X. Yang, T. Liu, A.J. Wang, S.L. Luo, *Chem. Eng. J.* 359 (2019) 894–901.
- [49] A.H. Nethercot, *Phys. Rev. Lett.* 33 (1974) 1088–1091.
- [50] S. Chen, Y. Hu, S. Meng, X. Fu, *Appl. Catal. B: Environ.* 150–151 (2014) 564–573.
- [51] H.J. Li, B.W. Sun, L. Sui, D.J. Qian, M. Chen, *Phys. Chem. Chem. Phys.* 17 (2015) 3309.
- [52] B. Peng, P.K. Ang, K.P. Loh, *Nano Today* 10 (2015) 128–137.
- [53] F. Dong, L. Wu, Y. Sun, M. Fu, Z. Wu, S.C. Lee, *J. Mater. Chem.* 21 (2011) 15171–15174.